Chapter 6

Measuring Vascular Permeability In Vivo

Eelco F.J. Meijer, James W. Baish, Timothy P. Padera, and Dai Fukumura

Abstract

Over the past decades, in vivo vascular permeability measurements have provided significant insight into vascular functions in physiological and pathophysiological conditions such as the response to pro- and anti-angiogenic signaling, abnormality of tumor vasculature and its normalization, and delivery and efficacy of therapeutic agents. Different approaches for vascular permeability measurements have been established. Here, we describe and discuss a conventional *2D* imaging method to measure vascular permeability, which was originally documented by Gerlowski and Jain in 1986 (Microvasc Res 31:288–305, 1986) and further developed by Yuan et al. in the early 1990s (Microvasc Res 45:269–289, 1993; Cancer Res 54:352–3356, 1994), and our recently developed *3D* imaging method, which advances the approach originally described by Brown et al. in 2001 (Nat Med 7:864–868, 2001).

Key words Vascular permeability, Intravital fluorescence microscopy, Vascular normalization, Multiphoton microscopy

1 Introduction

Measurements of transvascular transport have been proven invaluable in studying numerous in vivo processes and their regulation, including pro- and anti-angiogenic signaling, as well as vascular abnormalities and their putative normalization in disease states like cancer and inflammation [5]. It has been shown that abnormal tumor vasculature can be remodeled towards a more normal phenotype ("normalization") by restoring the proper balance of pro- and anti-angiogenic signaling pathways, improving vascular function [6], and delivery of therapeutics [7]. There are two different types of transport for molecules to extravasate across the blood vessel wall—convection and diffusion [5]. Convection is an active transport defined by a driving force–pressure gradient and a resistance–hydraulic conductivity such that $\text{Convection} = L_p\, S\left[\left(P_v \quad P_i\right) \quad s\left(p_v \quad p_i\right)\right]$, where L_p = hydraulic conductivity of vessel ($cm^4/s\text{-}mmHg$); S = surface area per unit volume (cm^2/cm^3), P_v; P_i = vascular and interstitial

Josie Ursini-Siegel and Nicole Beauchemin (eds.), *The Tumor Microenvironment: Methods and Protocols*, Methods in Molecular Biology, vol. 1458, DOI 10.1007/978-1-4939-3801-8_6,

pressures; s = osmotic reflection coefficient, p_v; and p_i = vascular and interstitial osmotic pressures (mmHg). On the other hand, diffusion is a passive transport defined by concentration gradients and permeability such that Diffusion = $PS\left(C_v \quad C_i\right)$, where P = vascular permeability (cm/s); S = surface area per unit volume (cm^2/cm^3), C_v; and C_i = concentrations in vascular and interstitial space (mol/cm^3). Tumor vessels are leaky which elevates tumor interstitial fluid pressure. While the extravagated fluid can escape (ooze out) from the tumor periphery, it builds up inside the tumor mass. Therefore, the pressure gradient across a vessel wall is diminished in tumors making convective transport less important and diffusion the dominant transport mechanism in solid tumors [8]. In this chapter, we discuss tumor transvascular transport measurements which is referred to as the effective permeability. It includes the dominant diffusive component (intrinsic permeability) as well as the less important convective component [5]. Effective permeability is a principal parameter to understand functionality of blood vessels and especially in tumors, one of the most important parameters [5, 6].

Early methods for estimating vascular permeability using *2D* imaging data were formulated by Gerlowski and Jain in 1986 [1] and further developed in the early 1990s by Yuan et al. [2, 3]. This approach relies on the estimates derived from temporal alteration in total fluorescence intensity as well as vascular morphologies obtained from superficial aspects of tissue using intravital fluorescence microscopy. Around a decade later, a *3D* approach was developed by Brown et al. [4] using multiphoton microscopy [9]. This advanced optical technique allows determining fluorescence intensity gradients surrounding *individual* vessels to calculate local permeability with high spatial resolution.

Both the *2D* and *3D* vascular permeability measurement methods are based on the same general principles. If pressure-driven transport can be neglected in a region of interest (ROI), as is often the case in disease states such as tumors, the apparent vascular permeability P may be calculated from $P = J / S \quad C$, where J is the rate at which a solute material is transported across a membrane of area S due to the concentration difference across the membrane ΔC. The most common approaches to measuring J, S, and ΔC involve three related but distinct steps. The first is establishment of a known concentration difference between the inside and outside of one or more blood vessels (ΔC). Image-based methods are used to observe the concentrations inside and outside of the vessel wall where the concentration is taken to be proportional to the observed fluorescence level. Right after injecting fluorescent material, the concentration outside the vessel wall should be zero. Secondly, the surface area of the blood vessel must be estimated (S). Estimates of the surface area are derived from the analysis of the vascular architecture in the image. If the vessel can be assumed to be cylindrical,

the surface can be estimated from the length and diameter of the vessel. Alternatively, a pixel or voxel counting technique can be employed to estimate the surface area if the vascular architecture is identified in *3D*. Thirdly, the transport rate is determined from changes in the fluorescence intensity of the tissue over time. Typically, the intravascular and extravascular spaces are taken to be different control volumes separated by the membrane. If we assume that all of the fluorescent material leaving the blood vessel through the vessel wall can be observed in the extravascular space of the ROI,

we can represent flux as $J = \frac{d}{dt}\int_{V_{ex}} C_{ex}\, dV$. However, for this equation to be strictly valid the boundary of the ROI must not offer an alternative route in or out. Such conditions might be well approximated if the blood vessels are relatively distant from the ROI boundary, or the boundary is sufficiently typical of adjacent ROIs such that material loss at the boundary is balanced by material gain. Accurately determining the flux has proven the biggest challenge.

The *2D* approach from Yuan et al. has proven valuable for measuring vascular permeability using the principles described above (*see* Table 1 for examples of *2D* permeability measurements). This technique, however, has several limitations because of its many assumptions. Because this method is in *2D*, the surface area-to-volume ratio of vessels collected from a single defocused plane on the surface is used to approximate the ratio of vessels in the entire ROI that is being imaged. Also, in a fluorescence image, the vessel diameter will appear larger than its true value because of light scattering, which needs to be corrected for. The actual in vivo tissue depth of the ROI being measured may also vary per tissue and tumor, depending on the cellular content and fluorescent material used. In addition, the vessels are assumed to be of cylindrical shape to be able to estimate the surface area of the blood vessels. Lastly, any fluorescent material leaking out from tissue surrounding the ROI and residing on top of the tissue will incorrectly increase calculated vascular permeability value, leading to measurement error in some samples.

The *3D* method using multiphoton microscopy—which can achieve greater imaging depths when compared to single-photon intravital imaging techniques—described in Brown et al. addressed many of the issues described above, but has some disadvantages on its own (*see* Table 1 for examples of *3D* permeability measurements). This method requires an accurate vessel mask and the quality of the multiphoton microscopy images dominates how accurate the vessel masking is at greater tissue depths. However, the actual tissue depth where light is collected is known using this method and the surface area-to-volume ratio is more realistic than the *2D* method. In addition, light scattering adjustments as well as hematocrit value and

Table 1
Examples of *2D* and *3D* method permeability measurements in the E.L. Steele Laboratories

Site	Tumor/model	Animal	Treatment/manipulation	Probes	*2D* methods	*3D* method	References
Brain (cranial window)	U87	Nude/SCID	Anti-VEGF/R2/Ang2/PlGF	BSA	$0.7–3.8\times10^{-7}$ cm/s	$0.4–2.5\times10^{-7}$ cm/s	[14–19]
	U87/MCaIV	SCID	VEGF-GFP imaging	100 and 500 nm QD-NP	NP and VEGF co-localize		[20]
	U87/GL261	*Rag-1-/-/-* SCID	nNOS KD/nNOS inhibitor	BSA	$0.3–7.8\times10^{-7}$ cm/s		[21]
	HGL21	SCID	VEGF		$0.11–4.3\times10^{-7}$ cm/s		[14, 22]
	HCaI/Shionogi/MCaIV	SCID		100–550 nm NP	HCaI 210-380, Shionogi 100–380, MCaIV 380–550 nm		[23]
	MCaIV	C3H/SCID		BSA	$1.9–2.9\times10^{-7}$ cm/s		[14]
	R3230AC	Fisher Rat			1.7×10^{-7} cm/s		[14]
	MDA-MB-361HK	SCID	Anti-HER2		$2.7–8.0\times10^{-7}$ cm/s		[24]
	ZR75-1	SCID			1.2×10^{-7} cm/s		[25]
	Tissue-engineered vessels	SCID	HUVEC, CB-EPC + 10T1/2		$0.5–4.4\times10^{-7}$ cm/s		[26–28]
			hiPSC-EC + 10T1/2			$0.2–15\times10^{-7}$ cm/s	[29]
	Normal cranium				$0.2–0.8\times10^{-7}$ cm/s		[22, 26]
Cerebellum window	D283-MED	SCID	Anti-PlGF	BSA		$1.2–3.1\times10^{-7}$ cm/s	[30]
Breast (mammary fat pad window)	E0771/4T1	SCID	Low dose anti-VEGFR2	12, 60, 125 nm Qd NP		0.01–0.45 μm/s Transvascular flux	[31, 32]
	E0771	SCID		Rod, sphere-shape Qd NP		0.04–0.17 μm/s Transvascular flux	[33]
	E0771/MCaIV	SCID		Neutral and negative charge Qd NPs		$0.3–5.0\times10^{-4}$ μm/s Transvascular flux	[34]
	4T1	Nude	VE-PTP inhibitor	BSA		0.1–1.8-fold	[35]
	ZR75-1	SCID		BSA	3.2×10^{-7} cm/s		[25]

Liver (acute)	LS174T	SCID		BSA	4.8×10^{-7} cm/s		[36]
	Normal liver				0.27×10^{-7} cm/s		
Pancreas (abdominal wall window)	Panc-1	SCID		BSA	3.1×10^{-7} cm/s		[37]
	Normal pancreas				0.5×10^{-7} cm/s		
Skin (dorsal skin chamber)	LS174T	SCID	Anti-VEGF, NOS inhibitor	BSA	$1.2–6.0\times10^{-7}$ cm/s		[2, 3, 15, 36, 38]
				90 nm NP	0.2×10^{-7} cm/s		[3]
				Mr. 24,000 (Fc) to 160,000 (IgG)	$1.5–5.7\times10^{-7}$ cm/s		[39]
				BSA	Single vessel permeability		[40]
	MCaIV	C3H/SCID	NOS inhibitor, anti-VEGFR2, PDT		$1.3–2.6\times10^{-7}$ cm/s	3.5×10^{-7} cm/s	[4, 38, 41, 42]
	Shionogi	SCID	Castration		$0.6–3.4\times10^{-7}$ cm/s		[43]
	HCaI/Shionogi/ MCaIV			100–2000 nm NP	HCaI 380-550, Shionogi 200–380, MCaIV 1200–2000 nm		[23]
	Mu89 melanoma			12, 60, 125 nm QD-NP		10–250 μm penetration	[44]
	T241		VEGF-C, anti-VEGFR2, VFGF-null	BSA	$0.5–4.4\times10^{-7}$ cm/s		[45]
	hES-teratoma		VEGF KO/HIF-1 KO		$1.3–3.1\times10^{-7}$ cm/s		[46]
	Normal skin				$0.3–0.7\times10^{-7}$ cm/s		[22]
Ear (*in situ*)	Spontaneous SCC	*Pol η−/−*		BSA	$1.2–9.4\times10^{-7}$ cm/s		[47]

4T1 murine breast cancer, *Ang2* angiopoietin 2, *BSA* bovine serum albumin, *CB-EPC* cord blood endothelial progenitor cell, *D283-MED* human medulloblastoma, *E0771* murine breast cancer, *GL261* murine glioma, *HCaI* murine hepatoma, *HER2* human epidermal growth factor receptor 2, *hES* human embryonic stem ells, *hiPSC* human induced pluripotent stem cell, *HUVEC* human umbilical vein endothelial cell, *LS174T* human coon cancer, *Mu89* human melanoma, *nNOS* neuronal nitric oxide synthase, *Panc-1* human pancreatic cancer, *PDT* photodynamic therapy, *PlGF* placenta growth factor, *QD-NP* quantum dot-nanoparticle, *R3230AC* rat breast cancer (rat mammary), *SCC* squamous cell carcinoma, *SCID* severe combined immunodeficient mice, *Shionogi* murine androgen-dependent cancer, *T241* murine fibrosarcoma, *U87* human glioma, *VEGF* vascular endothelial growth factor, *VEGFR2* VEGF receptor 2, *VE-PTP* vascular endothelial protein tyrosine phosphatase, *ZR75-1* human breast cancer

cylindrical vessel shape assumptions are not needed. Fluorescent material residing on top of the tissue can also be selectively avoided.

The formula used by Brown et al. calculates vascular permeability (P) in cm/s as $P = \lim_{t\to 0} \frac{\delta}{\delta t} \frac{\int_{r=R}^{\infty} F(r) r\, dr}{(F_v - F_i) R}$. Derivatives should be d/dt not lower case delta. This formula, however, is not strictly correct except under fairly restrictive conditions that may not be generally met. Correct use of this method requires that a roughly cylindrical region exists around a vessel that is influenced only by the vessel of interest during the time that is used for permeability calculation. In vivo, however, this cylindrical region is generally not present because the ROI may include multiple—tortuous—vessels in close vicinity. Vessels may also be present near the edges of the ROI. Altogether, this *3D* method yields a more realistic measurement of vascular permeability.

A recommended alternative approach would be to use a box-shaped ROI, using $P = \frac{\frac{\delta}{\delta t} \int_{Vext} F(\vec{r})\, dV}{S(F_v - F_i)}$ Derivatives should be d/dt as used in Kesler et al. [10]. In this approach, the voxels are segmented into three categories, namely those inside the vessel, those on the vessel wall, and those outside the vessel. For calculating vascular permeability, all vessels are mathematically considered as a single vessel. A downside of this approach is that permeability differences among single vessels cannot be estimated. However, the mean over all vessels should be very well estimated if the vessel masking is adequate.

The experimental setup of the *2D* method developed by Yuan et al. and our recommended alternative *3D* approach to measure vascular permeability in vivo are discussed in detail below. If executed properly, our recommended *3D* approach should yield more accurate and reliable in vivo vascular permeability measurements than the other methods discussed. The *3D* permeability measurements, however, rely heavily on an accurate vessel masking and while our vessel masking described below is fairly accurate in a range of tissues with high signal-to-noise ratio and low auto-fluorescence, a different approach for vessel masking may be more practically robust if images are obtained with lower signal-to-noise ratio or if there is high auto-fluorescence. Comparison between permeability measurements obtained with the same method can be safely made. However, the comparison of permeability measurements between different methods should be made with caution. There should be a common comparator such as measurements performed in the same tumor model with the same condition

(i.e., size, control treatment) in order to interpret the data properly. As discussed above, the difference in surface area-to-volume ratio estimation of multiple vessels in a similar ROI between the *2D* and *3D* methods will tend to result inherently lower calculated permeability values in the *2D* method as compared to that in the *3D* method. Hence, for the comparison purpose, the *3D* measurement raw data should be converted to *2D* data before the analysis. Finally, examples of vascular permeability measurements from the E.L. Steele Laboratories using *2D* and *3D* methods described by Yuan et al. and Brown et al., respectively, are summarized in Table 1.

2 Materials

1. General materials: Heating pad or similar device.
2. Ketamine/xylazine mixture 90 mg/9 mg per kg body weight.
3. Fluorescent molecules: 1% 2,000,000 mol. wt. fluorescein isothiocyanate (FITC)-dextran, 1% tetramethylrhodamine-bovine serum albumin (BSA), and 1% FITC-BSA.
4. $30^{1/2}$ gauge needles.
5. PE10 Polyethylene Tubing.
6. ½ cc U-100 $28^{1/2}$ gauge insulin syringes.
7. Graticule slides.

2.1 Microscope Setup Measuring Vascular Permeability in Mice Using 2D Method

1. The tracer molecules used in this method are 100 μL per 25 g body weight 1% 2,000,000 mol. wt. FITC-dextran and 1% tetramethylrhodamine-BSA.
2. A fluorescence intravital microscope (*see* Fig. 1) is used with a long-working-distance 20 × 0.40 NA objective and a fluorescence filter set suitable for FITC and rhodamine, connected to an intensified charge-coupled device (CCD) video camera and photomultiplier tube.
3. A computer is used to capture the output.
4. The microcirculation is epi-illuminated by a 100-W mercury lamp.
5. A 50% neutral density filter and a heat absorption filter were put in the epi-illumination pathway to prevent overheating of tissue.

2.2 Microscope Setup Measuring Vascular Permeability in Mice Using 3D Method

1. The tracer molecule used in this method is 100 μL per 25 g body weight 1% FITC-BSA.
2. The multiphoton microscope (*see* Fig. 1) consists of a mode-locked Ti:sapphire laser and an x–y laser scanner purchased as described previously [4]. A Pockels cell is used to allow for rapid modulation of laser intensity.

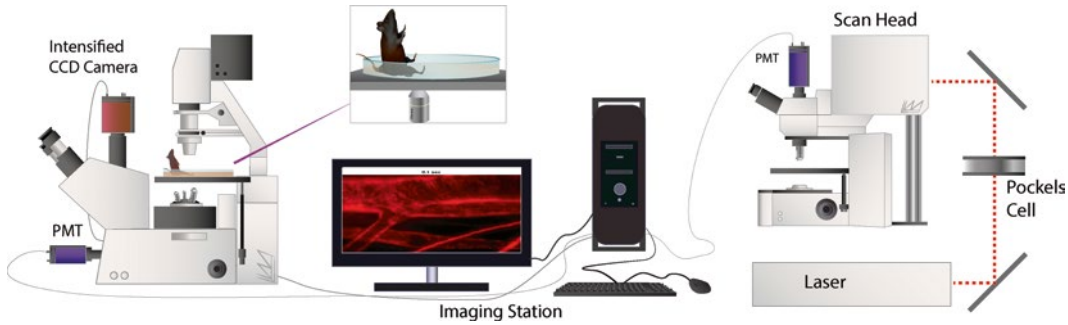

Fig. 1 Schematic representation of the fluorescence intravital microscope (*left*) and multiphoton microscope (*right*) setups. Fluorescence intravital microscopy and multiphoton microscopy are used for *2D* and *3D* method permeability measurements, respectively. Inverted microscope (*left*) with popliteal lymph node/lymphatics imaging setup is shown. Both inverted and upright (*right*) microscope with appropriate animal models can be used for the permeability measurements. *CCD* cooled coupled device, *PMT* photomultiplier tube. This figure was generously drawn by Dr. Lance L. Munn, E.L. Steele Laboratories, Boston, MA

3. The system also requires non-descanned photomultiplier tubes (PMT), a dichroic beam splitter, a digital image and analysis station, and a computer with image acquisition software. We use a 20×0.95 NA or 25×1.05 NA water-immersion objective (Olympus) and a 525DF100 filter (Chroma) suitable for FITC.

3 Methods

3.1 Measuring Vascular Permeability in Mice Using *2D* Method

General comment: Make sure that the microscope is in complete darkness when imaging.

1. Anesthetize the mouse with a ketamine/xylazine mixture 90 mg/9 mg per kg body weight. Maintain the animal's core body temperature using a heating pad or similar device.
2. Insert a $30^{1/2}$ gauge needle into a tail vein, connected to PE10 Polyethylene Tubing and a ½cc U-100 $28^{1/2}$ gauge insulin syringe filled with 100 μL per 25 g body weight 1% 2,000,000 mol. wt. FITC-dextran. Also prepare an insulin syringe filled with 100 μL per 25 g body weight 1% tetramethylrhodamine-BSA.
3. Inject the FITC-dextran (MW 2,000,000 or more). Flush the Polyethylene Tubing with a small amount of physiologic saline for intravenous infusion and leave the needle in the tail vein (*see* **Note 1**). FITC-dextran is used for vessel marking (*see* **step 10**). It does not easily extravasate into the surrounding tissue due to its large molecular weight.
4. Place the mouse and the area to be studied under the intravital fluorescence microscope, equipped with the fluorescence fil-

ter set for rhodamine and FITC and a 100-W mercury lamp (*see* **Note 2**).

5. Acquire an image of the vessels in the area to be studied using the CCD camera. Do this by using the fluorescence filter for FITC (*see* **Note 3**). It is important to settle the location of permeability measurement and focus target blood vessels using FITC-dextran image as there is little room of adjustment once the permeability measurements start (*see* **step 7**).
6. Set the fluorescence filter to rhodamine. Use the photomultiplier tube to acquire background signal for several seconds and make sure that the system is fully operational.
7. Attach the insulin syringe containing tetramethylrhodamine-BSA. Start measuring the tissue fluorescence using the PMT and subsequently inject the tetramethylrhodamine-BSA. Flush the Polyethylene Tubing with a small amount of physiologic saline for intravenous infusion. Do not exceed 10 s of measuring to avoid photo-damage of the tissue and photo-bleaching of the fluorescent molecules (*see* **Note 4**). Tetramethylrhodamine-BSA will start leaking out into the surrounding tissue immediately. By using narrow band-pass filters the PMT, fluorescence of tetramethylrhodamine-BSA, and FITC-dextran are clearly separated. Different combinations of two different fluorophores can be used for permeability measurements as long as fluorescence spectra are reasonably separated and with the proper sets of band-pass filters. In general, longer wavelength is preferred for permeability measurement due to reduced auto-fluorescence and tissue penetration.
8. Repeat 10 s of signal acquisition every 2 min for up to 20 min.
9. After the last signal acquisition, acquire a second image of the vessels in the area studied using the fluorescence filter for FITC and the CCD camera. Compare with the image taken at **step 5** and confirm the tissue had no x, y, or z shift.
10. Using the images and measurements gathered, vascular permeability (P) can be calculated in cm/s as $P=(1-\mathrm{HT})V/S(1/(I_0-I_b)\cdot dI/dt+1/K)$, where HT is the tissue hematocrit estimated to be 0.19 in tumors [3, 11] and 0.46 in the systemic circulation [12], I is the average fluorescence intensity of the whole image, I_0 is the value of I immediately after the filling of all vessels by tetramethylrhodamine-BSA, I_b is the background fluorescence intensity, and K is the time constant of plasma clearance estimated to be 9.1×10^3 s for BSA [3]. The slope of the measurements plotted over time should be normalized, where dI/dt becomes $(dI/dt)/(I_0-I_b)$. V and S are the total volume and surface area of vessels within the tissue volume covered by the surface image, respectively. The volume-to-sur-

face ratio is calculated as $\frac{V}{S} = \sum_{n=1}^{M} L_n d_n^2 / \sum_{n=1}^{M} 4 d_n L_n$ where *dn* is the diameter of the *n*th vessel and *Ln* is the length of the *n*th vessel corrected by a factor of 0.79 for light scattering in the tissue [3]. These vessel diameters and lengths can be manually calculated from the acquired image of the vessels in the area to be studied after injecting FITC-dextran (*see* **Note 5**).

3.2 Measuring Vascular Permeability in Mice Using 3D Method

General comment: Make sure that the microscope is in complete darkness when imaging.

1. Make sure that your multiphoton setup is working correctly before you anesthetize your mouse. Use fluorescence filters adequate for the material you will be using, in this case FITC-BSA. We use a 525DF100 filter. Set Ti-sapphire laser wavelength to 780 nm. Set laser power to 60 mW.
2. Anesthetize the mouse with a ketamine/xylazine mixture 90 mg/9 mg per kg body weight. Maintain the animal's core body temperature using a heating pad or similar device.
3. Insert a $30^{1/2}$ gauge needle into a tail vein, connected to PE10 Polyethylene Tubing and a ½cc U-100 $28^{1/2}$ gauge insulin syringe filled with 100 µL per 25 g body weight 1% FITC-BSA.
4. Place the mouse and the area to be studied under the multiphoton microscope objective. We use a 20×0.95 NA or 25×1.05 NA water-immersion objective. Set the focus on the most superficial vasculature you can find in the area of interest and make sure that the water between tissue and objective is not leaking.
5. Inject the FITC-BSA. Flush the Polyethylene Tubing with a small amount of physiologic saline for intravenous infusion (*see* **Note 6**).
6. Start imaging 30 s after injecting FITC-BSA. Arteries show fluorescence within seconds after injection; veins can take somewhat longer. We use the slowest acquisition to get best quality images, 256×256 voxels, 74 *z* slices, and steps of 1.84 µm obtained with a 25× water-immersion objective. For a 20× objective, use *z* steps of 2.76 µm (*see* **Note 7**).
7. Acquire *z* stacks for up to 20 min (*see* **Note 8**).
8. For image analysis, we recommend a box-shaped ROI approach containing multiple vessels. Use software to segment voxels into three categories: those inside the vessel, those on the vessel wall, and those outside the vessel (*see* Fig. 2). Calculate vas-

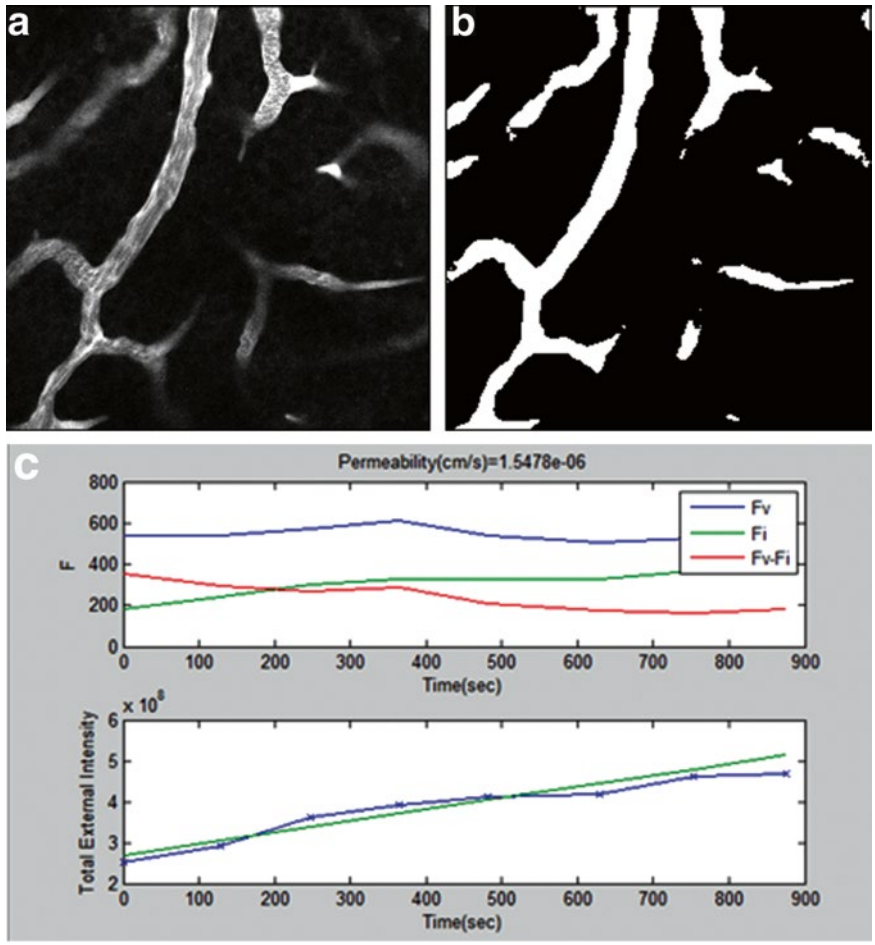

Fig. 2 Example of *3D* method data analysis. (**a**) Single slice from a multiphoton image *z* stack of tumor vasculature. (**b**) Vessel masking from slice presented at **a** using method "*Li*" thresholding in ImageJ. (**c**) *Right-top graph* shows MATLAB results from the same *z* stack (44 out of 74 slices, $z \approx 81$ μm, 8 time points over 15 min, images not shown) showing a vascular permeability of 1.55×10^{-6} cm/s. *Right-bottom graph* depicts the total external intensity (F_e, *blue line*) being the total fluorescence from all exterior points including those on the wall and the straight line (*green line*) being the slope estimated from the first 6 time points to which the *blue line* theoretically should closely adhere to. *F* fluorescence intensity, F_v mean fluorescence from the interior voxels, F_i mean fluorescence from the vessel wall voxels

cular permeability (P) as

$$P = \frac{(\text{voxel size}) \times \text{Slope of } F_e \text{ over time}}{(n_{wall}) \times \text{Mean of } (F_v - F_i)}$$

where n_{wall} is the number of voxels making up the vessel walls, F_e is the total fluorescence from all exterior points including those on the wall, F_v is the mean fluorescence from the interior voxels, and F_i is the mean fluorescence from the vessel wall voxels (*see* **Note 9**).

4 Notes

1. Insulin syringes are precise and have little syringe dead space.
2. We prefer using a chronic window to keep the area to be studied in place and allow for chronic imaging without serial laparotomies and breathing artifacts [13].
3. Take an image with maximum gain that the camera can handle without damaging it or before switching off. Do not adjust offset or other settings; you can do this later with image processing software.
4. Leave the needle in the tail vein attached to the tubing and syringe to prevent blood loss.
5. Use a graticule slide to know the actual size of the area and vessels you are measuring. Use μm for V/S and K in seconds.
6. Make sure that the area you are imaging is clean. If you are using imaging windows with a cover slip, replace the glass cover slip before imaging if needed. If there is water leakage, check if the cover slip is intact and well secured or replace the cover slip. Also, be particularly careful to prevent collision between your objective and anything that can damage it.
7. Do not adjust the gain, offset, etc. Similar modifications can be done after imaging with off-line processing while keeping the best quality raw data. We would recommend gathering more z slices than you need to be able to correct for any z shift you might experience over time. Moreover, check your data for pixel saturation. If you are seeing saturation in the fluorescence intensity in your data, lower the photomultiplier tube power or alternatively lower laser power in future experiments; your data will be incorrect and hence (partly) useless otherwise.
8. Stay alert for xy shifts during imaging; you can manually adjust these in between data acquisition or use off-line processing to correct for this later. If you are seeing intensity loss of the vessels in the field of view, make sure that there is enough water between the tissue and the objective. We recommend leaving a syringe with water in the vicinity of your objective.
9. We use ImageJ (1.47v, *NIH*) for vessel masking and MATLAB (R2015b, *MathWorks*) for further data analysis. Use earliest data stacks acquired for vessel masking to obtain the most accurate mask. Data stacks are converted to binary (ImageJ > Process > Binary > Make Binary > Method "Li") and a median filter (Process > Filter > Median > Radius 1 pixel) is subsequently used to remove noise and smoothen blood vessel lumen but not the vessel wall. The *MATLAB* script is not added here due to page limitations but is available upon request.

Acknowledgements

We would like to thank Echoe Bouta, Cheryl Cui, Nir Maimon, Lance L. Munn, and Rakesh K. Jain from the E.L. Steele Laboratories and Cedric Blatter and Benjamin Vakoc from the Wellman Center for Photomedicine (Massachusetts General Hospital, USA) for insightful discussions and intellectual input. We would like to thank Lance L. Munn for his help with illustrations and Cedric Blatter for his tremendous help with vessel masking and MATLAB coding for the *3D* method. This study was supported by the National Institutes of Health grants P01-CA 080124 (DF), DP2-OD008780 (TPP) and R01-HL128168 (TPP, JWB).

References

1. Gerlowski LE, Jain RK (1986) Microvascular permeability of normal and neoplastic tissues. Microvasc Res 31:288–305
2. Yuan F, Leunig M, Berk DA, Jain RK (1993) Microvascular permeability of albumin, vascular surface area, and vascular volume measured in human adenocarcinoma LS174T using dorsal chamber in SCID mice. Microvasc Res 45:269–289
3. Yuan F, Leunig M, Huang SK, Berk DA, Papahadjopoulos D, Jain RK (1994) Microvascular permeability and interstitial penetration of sterically stabilized (stealth) liposomes in a human tumor xenograft. Cancer Res 54:352–3356
4. Brown EB, Campbell RB, Tsuzuki Y, Xu L, Carmeliet P, Fukumura D, Jain RK (2001) In vivo measurement of gene expression, angiogenesis and physiological function in tumors using multiphoton laser scanning microscopy. Nat Med 7:864–868
5. Jain RK (1987) Transport of molecules across tumor vasculature. Cancer Metastasis Rev 6:559–593
6. Jain RK, Munn LL, Fukumura D (2002) Dissecting tumour pathophysiology using intravital microscopy. Nat Rev Cancer 2:266–276
7. Chauhan VP, Jain RK (2013) Strategies for advancing cancer nanomedicine. Nat Mater 12:958–962
8. Baxter LT, Jain RK (1989) Transport of fluid and macromolecules in tumors. I. Role of interstitial pressure and convection. Microvasc Res 37:77–104
9. Denk W, Strickler JH, Webb WW (1990) Two-photon laser scanning fluorescence microscopy. Science 248:73–76
10. Kesler CT, Pereira ER, Cui CH, Nelson GM, Masuck DJ, Baish JW, Padera TP (2015) Angiopoietin-4 increases permeability of blood vessels and promotes lymphatic dilation. FASEB J 29:3668–3677
11. Brizel DM, Klitzman B, Cook JM, Edwards J, Rosner G, Dewhirst MW (1993) A comparison of tumor and normal tissue microvascular hematocrits and red cell fluxes in a rat window chamber model. Int J Radiat Oncol Biol Phys 25:269–276
12. Schuler B, Arras M, Keller S, Rettich A, Lundby C, Vogel J, Gassmann M (2010) Optimal hematocrit for maximal exercise performance in acute and chronic erythropoietin-treated mice. Proc Natl Acad Sci U S A 107:419–423
13. Brown E, Munn LL, Fukumura D, Jain RK (2010) In vivo imaging of tumors. Cold Spring Harbor Protoc 2010(7):pdb.prot5452
14. Yuan F, Salehi HA, Boucher Y, Vasthare US, Tuma RF, Jain RK (1994) Vascular permeability and microcirculation of gliomas and mammary carcinomas transplanted in rat and mouse cranial windows. Cancer Res 54:4564–4568
15. Yuan F, Chen Y, Dellian M, Safabakhsh N, Ferrara N, Jain RK (1996) Time-dependent vascular regression and permeability changes in established human tumor xenografts induced by an anti-vascular endothelial growth factor/vascular permeability factor antibody. Proc Natl Acad Sci U S A 93:14765–14770
16. Winkler F, Kozin SV, Tong RT, Chae SS, Booth MF, Garkavtsev I et al (2004) Kinetics of vascular normalization by VEGFR2 blockade governs brain tumor response to radiation: role of oxygenation, angiopoietin-1, and matrix metalloproteinases. Cancer Cell 6:553–563

17. Xu L, Cochran DM, Tong RT, Winkler F, Kashiwagi S, Jain RK, Fukumura D (2006) Placenta growth factor overexpression inhibits tumor growth, angiogenesis, and metastasis by depleting vascular endothelial growth factor homodimers in orthotopic mouse models. Cancer Res 66:3971–3977
18. Kamoun WS, Ley CD, Farrar CT, Duyverman AM, Lahdenranta J, Lacorre DA et al (2009) Edema control by cediranib, a vascular endothelial growth factor receptor-targeted kinase inhibitor, prolongs survival despite persistent brain tumor growth in mice. J Clin Oncol 27:2542–2552
19. Chae SS, Kamoun WS, Farrar CT, Kirkpatrick ND, Niemeyer E, de Graaf AM et al (2010) Angiopoietin-2 interferes with anti-VEGFR2-induced vessel normalization and survival benefit in mice bearing gliomas. Clin Cancer Res 16:3618–3627
20. Stroh M, Zimmer JP, Duda DG, Levchenko TS, Cohen KS, Brown EB et al (2005) Quantum dots spectrally distinguish multiple species within the tumor milieu in vivo. Nat Med 11:678–682
21. Kashiwagi S, Tsukada K, Xu L, Miyazaki J, Kozin SV, Tyrrell JA et al (2008) Perivascular nitric oxide gradients normalize tumor vasculature. Nat Med 14:255–257
22. Monsky WL, Fukumura D, Gohongi T, Ancukiewcz M, Weich HA, Torchilin VP et al (1999) Augmentation of transvascular transport of macromolecules and nanoparticles in tumors using vascular endothelial growth factor. Cancer Res 59:4129–4135
23. Hobbs SK, Monsky WL, Yuan F, Roberts WG, Griffith L, Torchilin VP, Jain RK (1998) Regulation of transport pathways in tumor vessels: role of tumor type and microenvironment. Proc Natl Acad Sci U S A 95:4607–4612
24. Izumi Y, Xu L, di Tomaso E, Fukumura D, Jain RK (2002) Tumour biology: herceptin acts as an anti-angiogenic cocktail. Nature 416:279–280
25. Monsky WL, Mouta Carreira C, Tsuzuki Y, Gohongi T, Fukumura D, Jain RK (2002) Role of host microenvironment in angiogenesis and microvascular functions in human breast cancer xenografts: mammary fat pad versus cranial tumors. Clin Cancer Res 8:1008–1013
26. Fukumura D, Gohongi T, Kadambi A, Izumi Y, Ang J, Yun CO et al (2001) Predominant role of endothelial nitric oxide synthase in vascular endothelial growth factor-induced angiogenesis and vascular permeability. Proc Natl Acad Sci U S A 98:2604–2609
27. Koike N, Fukumura D, Gralla O, Au P, Schechner JS, Jain RK (2004) Tissue engineering: creation of long-lasting blood vessels. Nature 428:138–139
28. Au P, Daheron LM, Duda DG, Cohen KS, Tyrrell JA, Lanning RM et al (2008) Differential in vivo potential of endothelial progenitor cells from human umbilical cord blood and adult peripheral blood to form functional long-lasting vessels. Blood 111:1302–1305
29. Samuel R, Daheron L, Liao S, Vardam T, Kamoun WS, Batista A et al (2013) Generation of functionally competent and durable engineered blood vessels from human induced pluripotent stem cells. Proc Natl Acad Sci U S A 110:12774–12779
30. Snuderl M, Batista A, Kirkpatrick ND, Ruiz de Almodovar C, Riedemann L, Walsh EC et al (2013) Targeting placental growth factor/neuropilin 1 pathway inhibits growth and spread of medulloblastoma. Cell 152:1065–1076
31. Chauhan VP, Stylianopoulos T, Martin JD, Popovic Z, Chen O, Kamoun WS et al (2012) Normalization of tumour blood vessels improves the delivery of nanomedicines in a size-dependent manner. Nat Nanotechnol 7:383–388
32. Chauhan VP, Martin JD, Liu H, Lacorre DA, Jain SR, Kozin SV et al (2013) Angiotensin inhibition enhances drug delivery and potentiates chemotherapy by decompressing tumour blood vessels. Nat Commun 4:2516
33. Chauhan VP, Popovic Z, Chen O, Cui J, Fukumura D, Bawendi MG, Jain RK (2011) Fluorescent nanorods and nanospheres for real-time in vivo probing of nanoparticle shape-dependent tumor penetration. Angew Chem 50:11417–11420
34. Han HS, Martin JD, Lee J, Harris DK, Fukumura D, Jain RK, Bawendi M (2013) Spatial charge configuration regulates nanoparticle transport and binding behavior in vivo. Angew Chem 52:1414–1419
35. Goel S, Gupta N, Walcott BP, Snuderl M, Kesler CT, Kirkpatrick ND et al (2013) Effects of vascular-endothelial protein tyrosine phosphatase inhibition on breast cancer vasculature and metastatic progression. J Natl Cancer Inst 105:1188–1201
36. Fukumura D, Yuan F, Monsky WL, Chen Y, Jain RK (1997) Effect of host microenvironment on the microcirculation of human colon adenocarcinoma. Am J Pathol 151:679–688
37. Tsuzuki Y, Mouta Carreira C, Bockhorn M, Xu L, Jain RK, Fukumura D (2001) Pancreas microenvironment promotes VEGF expression and tumor growth: novel window models for pancreatic tumor angiogenesis and microcirculation. Laboratory investigation. J Tech Methods Pathol 81:1439–1451
38. Fukumura D, Yuan F, Endo M, Jain RK (1997) Role of nitric oxide in tumor microcirculation. Blood flow, vascular permeability,

and leukocyte-endothelial interactions. Am J Pathol 150:713–725
39. Yuan F, Dellian M, Fukumura D, Leunig M, Berk DA, Torchilin VP, Jain RK (1995) Vascular permeability in a human tumor xenograft: molecular size dependence and cutoff size. Cancer Res 55:3752–3756
40. Lichtenbeld HC, Yuan F, Michel CC, Jain RK (1996) Perfusion of single tumor microvessels: application to vascular permeability measurement. Microcirculation 3:349–357
41. Dolmans DE, Kadambi A, Hill JS, Waters CA, Robinson BC, Walker JP et al (2002) Vascular accumulation of a novel photosensitizer, MV6401, causes selective thrombosis in tumor vessels after photodynamic therapy. Cancer Res 62:2151–2156
42. Tong RT, Boucher Y, Kozin SV, Winkler F, Hicklin DJ, Jain RK (2004) Vascular normalization by vascular endothelial growth factor receptor 2 blockade induces a pressure gradient across the vasculature and improves drug penetration in tumors. Cancer Res 64:3731–3736
43. Jain RK, Safabakhsh N, Sckell A, Chen Y, Jiang P, Benjamin L et al (1998) Endothelial cell death, angiogenesis, and microvascular function after castration in an androgen-dependent tumor: role of vascular endothelial growth factor. Proc Natl Acad Sci U S A 95:10820–10825
44. Popovic Z, Liu W, Chauhan VP, Lee J, Wong C, Greytak AB et al (2010) A nanoparticle size series for in vivo fluorescence imaging. Angew Chem 49:8649–8652
45. Kadambi A, Mouta Carreira C, Yun CO, Padera TP, Dolmans DE, Carmeliet P et al (2001) Vascular endothelial growth factor (VEGF)-C differentially affects tumor vascular function and leukocyte recruitment: role of VEGF-receptor 2 and host VEGF-A. Cancer Res 61:2404–2408
46. Tsuzuki Y, Fukumura D, Oosthuyse B, Koike C, Carmeliet P, Jain RK (2000) Vascular endothelial growth factor (VEGF) modulation by targeting hypoxia-inducible factor-1alpha→hypoxia response element→VEGF cascade differentially regulates vascular response and growth rate in tumors. Cancer Res 60:6248–6252
47. Hagendoorn J, Tong R, Fukumura D, Lin Q, Lobo J, Padera TP et al (2006) Onset of abnormal blood and lymphatic vessel function and interstitial hypertension in early stages of carcinogenesis. Cancer Res 66:3360–3364